Springer

Acta Mechanica Sinica

CrossMark click for updates

•RESEARCH PAPER•

Acta Mech. Sin., Vol. 38, 321251 (2022)
https://doi.org/10.1007/s10409-021-09058-x

Effects of bottom deflectors on aerodynamic drag reduction of a high-speed train

Wen Liu[1], Zhanling Ji[2*], Dilong Guo[2,3], Guowei Yang[2,3], Gaowei Zhou[1], and Kunhua Ren[1]

[1] *CRRC Industrial Academy Corporation Limited, Beijing 100070, China;*
[2] *Institute of Mechanics, Chinese Academy of Sciences, Beijing 100190, China;*
[3] *School of Engineering Science, University of Chinese Academy of Sciences, Beijing 100049, China*

Received August 18, 2021; accepted September 2, 2021; published online March 9, 2022

Inspired by the fact that bogies and bottom equipment generally contribute a great deal of aerodynamic drag to high-speed trains, this paper puts forward a simple method of mounting some small deflectors before and/or after the bogie cabins to optimize the underbody flow and reduce the aerodynamic drag of high-speed trains. The flow fields of the high-speed train models with and without bottom deflectors are numerically studied by the IDDES method. The effectiveness and further mechanism of the bottom deflectors on aerodynamic drag reduction are analyzed. It is demonstrated that the bottom deflectors could guide the underbody flow to the ground and prevent it from hitting on the bogies and bottom equipment of the train, resulting in a significant aerodynamic drag reduction effect. Moreover, the effects of different mounting locations of bottom deflectors on drag reduction are discussed as well, and an optimal mounting configuration with a drag reduction effect of up to about 12% is finally obtained. Nevertheless, the mounted deflector is also proved capable of significantly reducing the interference range of the underbody flow and reducing the slipstream of the train, which possesses a higher guarantee for the safety of railway workers and passengers waiting on the platforms. This work provides a new idea for aerodynamic drag reduction of high-speed trains, and is of great significance in energy conservation and consumption reduction.

High-speed train, Drag reduction, Bottom deflector, Bogie, Flow control

Citation: W. Liu, Z. Ji, D. Guo, G. Yang, G. Zhou, and K. Ren, Effects of bottom deflectors on aerodynamic drag reduction of a high-speed train, Acta Mech. Sin. **38**, 321251 (2022), https://doi.org/10.1007/s10409-021-09058-x

1. Introduction

In densely populated areas, such as China, Japan and Europe, high-speed railway has become an important means of transportation. According to China's medium-long term planning of high-speed railway, the total high-speed railway mileage is expected to reach about 38000 km by 2025 in China. Therefore, even only a small improvement of the performance of high-speed trains would lead to a significant impact on energy conservation and consumption reduction. Numerous studies [1-3] have shown that the aerodynamic drag of a high-speed train is proportional to the square of the running speed, and it can exceed 80% of the total drag under a train speed of 300 km/h even for a highly streamlined train. Therefore, under the background of continuously increasing the train speed, the large aerodynamic drag becomes one of the key technical challenges for the development of high-speed trains. Consequently, reduction of aerodynamic drag of high-speed trains is a key to reduce the tractive power and energy consumption, and consequently improve the economic benefits.

In the past decades, great efforts have been made to reduce the aerodynamic drag of high-speed trains. It has been acknowledged that the aerodynamic drag is dependent on the cross-sectional area of carriages, the length of train, the shapes of train's fore- and after-bodies, the roughness of train surface, and the geographical environment around the running train. At first, the most attention is paid to the shape optimization of the head car. Maeda et al. [4] and Li et al. [5]

*Corresponding author. E-mail address: jizhanling@imech.ac.cn (Zhanling Ji)
Executive Editor: Zhixiang Xiao

conducted wind tunnel tests and numerical simulations to extract the relationship between aerodynamic drag and head-shape parameters, and their results suggested that the aerodynamic drag is nearly independent of the ratio of the transition length to the model width, when this ratio exceeds a certain value. Du et al. [6] further studied the mapping relationships between the aerodynamic drag and other head-shape parameters. It was found that the maximum reduction of aerodynamic drag would not exceed 3%, even with an increase of the streamlined length from 8 m to 12 m, a decrease of the height of the nose's tip from 1 m to 0.5 m, or a decrease of the width of the nose cone from 1.2 m to 0.8 m for a mature high-speed train. Taking the aerodynamic forces as the optimization objectives and constructing a Kriging model based on the combination of a cross-validation method and the genetic algorithm, the aerodynamic force of the whole train was optimized by Yao et al. [7], and a maximum reduction of aerodynamic drag of 3.34% was finally obtained. Xu et al. [8] carried out multi-objective aerodynamic optimization of the streamlined shape of high-speed trains basing on the Kriging model, and a reduction of 7.2% of the whole drag of the optimized train has been achieved. In general, the currently used head shape had been optimized so well that its further improvement space may be relatively small. In other words, aerodynamic drag reduction of a high-speed train by optimizing the head-shape parameters has reached a bottleneck state. Consequently, it is imperative to look for other more effective methods to reduce the aerodynamic drags of high-speed trains.

Recently, flow control technologies have introduced some new concepts for high-speed train aerodynamic drag reduction. One of them is the bionic drag-reducing technology, which can achieve a considerable drag reduction effect by imitating the biological evolutionary process. Inspired by the scaly epithelium structures of marine animals, the body surface can be designed as non-smooth to reduce the viscous drag [9-12]. The detailed forms of these non-smooth surface structures can be micro-riblets, pits, bulges, etc. It has been found that the drag reduction effect is dependent on the specific structural parameters, array forms, and layout locations of these non-smooth structures. Similarly, imitating the elastic skin of dolphins, a flexible body surface performs a good effect on aerodynamic drag reduction as well [13,14]. As another flow control technology, a micro-blowing surface also bears significant potential in aerodynamic drag reduction for a high-speed train. For example, Shkvar et al. [15] achieved a drag reduction effect of 5.25% by setting a large number of micro-blowing holes on 70% surface of the head car. However, the above-mentioned drag-reducing technologies all require a large extent of modification to the train surface and consequently a large amount of engineering work, which is time-consuming and labor-consuming. Meanwhile, the operation and post-maintenance of these modified high-speed trains would face great challenges as well. Therefore, looking for other simpler ideas is rather imperative to the aerodynamic performance improvement of high-speed trains.

An investigation on aerodynamic drag percentages of different train parts, conducted by Nolte and Wurtenberger [16], showed that for a long high-speed train with many coaches, the large extent of exposure of accessorial parts of the train body, especially the bottom structures including bogies and wheels, contributes a large amount of aerodynamic drag to the train, even exceeding the contribution of the pressure drag of the head and trailing cars. This may be why the optimization of head shape has reached its bottleneck in aerodynamic drag reduction for a highly streamlined train, as mentioned above. This has brought us into the research of optimizing the bottom structures of high-speed trains to reduce the aerodynamic drag further. Suzuki et al. [17] optimized the aerodynamic performance of a high-speed train by installing bottom apron boards on the sides of the whole train or partially excluding the sides of the bogies, and the results showed that a considerable amount of aerodynamic drag reduction of the train was finally achieved. Moreover, the full-scale tests of a new ETR 500 high-speed train, conducted by Mancini et al. [18], revealed that the inclusion of bogie fairings reduced approximately 10% of overall aerodynamic drag compared with the standard configuration without fairings. Wang et al. [19] numerically studied the effects of the bogie cavity length on the aerodynamic performance of trains, and the results showed that the drag increased by 5.8% and 11.5%, with the bogie cavities being elongated by 20% and 40% of the wheelbase, respectively. Additionally, in the researches of Liu et al. [20], Zhang et al. [21], Gao et al. [22], Niu et al. [23], and Guo et al. [24], the importance of flow beneath the train body to the aerodynamic drag of a high-speed train had also been demonstrated.

In this paper, one kind of small and simple device, mounted on the bottom of the high-speed train, is proposed to optimize the bottom flow of the train and significantly reduce the aerodynamic drag. Specifically, some small and simple deflectors are set before and/or after the bogie cabins to smoothly guide the bottom high-speed flow to the ground, which previously would hit on the bogies and consequently lead to a large aerodynamic drag contribution. Taking the classical CRH380A high-speed train as an example, the flow fields of the regular train model without any bottom deflectors and some modified train models with bottom deflectors are numerically studied by the improved delayed detached eddy simulation (IDDES) method. Through the comparative analyses of the aerodynamic forces, pressure distributions, velocity distributions and slipstreams of the trains, the effectiveness and further the mechanism of the bottom deflectors on aerodynamic drag reduction of the train

are discussed. Moreover, the influences of the mounting location of the deflectors on drag reduction effects of the train are analyzed as well, and an optimal mounting solution is finally obtained.

2. Calculation models

2.1 High-speed train model

In this paper, the 1:1 scaled CRH380A high-speed train model, consisting of one head car, one middle car, and one trailing car is taken as an example, as shown in Fig. 1. It is a representative high-speed train in China for studying the flow around the train in experiments and numerical simulations. The designed train speed is $U_\infty = 350$ km/h. Since the aerodynamic drag induced by the bottom flow of the train is the focus of this study, the important structures such as the complicated bogies and inter-carriage gaps are considered, while other accessory parts such as pantographs and air conditionings are ignored. The train model is 78 m × 3.5 m × 3.378 m in length (L), height (H), and width (W), and the maximum cross-sectional area of each carriage is about S = 11.123 m^2. Notably, the length L refers to the longitudinal distance measured from the nose tip of the head car to that of the trailing car; the height H refers to the vertical distance measured from the bottom to the top of the middle carriage; the width W refers to the maximum width of the middle car. Define H as the characteristic length.

For simplicity of discussion in the later sections, the flow direction is defined as the positive direction of the x-axis, the vertical direction as the positive direction of the z-axis. Subsequently, the positive direction of the y-axis can be determined by the right-hand rule of the coordinate system, as shown in Fig. 1. Moreover, define the center of the train as $(x, y) = (0, 0)$ and the bottom end of the wheels as $z = 0$. Therefore, the locations of the bottom of the train body and the ground are respectively at $z = 0.2$ m and $z = -0.25$ m, while the coordinates of the front and back tips of the train are $(x, y, z) = (-39, 0, 1)$ m and $(39, 0, 1)$ m, respectively.

2.2 Geometry of the deflector

Inspired by the fact that the exposure of bogies and bottom equipment under the trains contribute a large amount of aerodynamic drag to a multi-car high-speed train, a simple method of mounting some small deflectors before and/or after the bogie cabins under the train is proposed. Taking the half of first bogie zone of the train as an example, the installation position of the bottom deflector is shown in Fig. 2a, and the detailed geometry of this designed deflector model, consisting of a windward side (C1) and a leeward side (C2), is schematically shown in Fig. 2b. To smoothly deflect the incoming flow, the windward side of the deflector is designed as an arc-shaped surface and tangent to the floor of the train body (or the bottom side of the train cowcatcher for the first bogie zone). Moreover, the leeward side is flat and connected to the apron boards and bogie cabin of the train, forming an angle of α ($\alpha = 30°$) between it and the floor of the train body. The height of the deflector along the z-axis is h, which should not be too large to ensure that the bottom end of the deflector is higher than the top of the rails, so as to prevent the deflector from contacting the rails. The length of the deflector is about $l_1 = 4.57 \times 10^{-2}H$ and $l_2 = 3.43 \times 10^{-2}H$, and the width in the spanwise direction (along the y-axis) is $w = 0.6H$, which is consistent with the width of the front or rear end of the bogie cabin.

2.3 Cases summary

To analyze the effectiveness of the designed bottom deflectors in an aerodynamic drag reduction of high-speed trains and further the effects of different installation positions, totally four train models are designed and simulated, including a prototype train model (the original CRH380A train model) without any bottom deflectors and three modified train models with different numbers of deflectors, as summarized in Table 1. The detailed locations of the installed bottom deflectors of the three modified train models are described in Fig. 3. Specifically, the modified train model has installed twelve bottom deflectors before and after the six

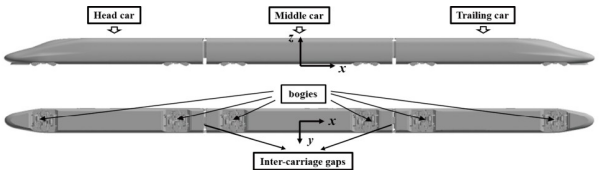

Figure 1 CRH380A high-speed train model.

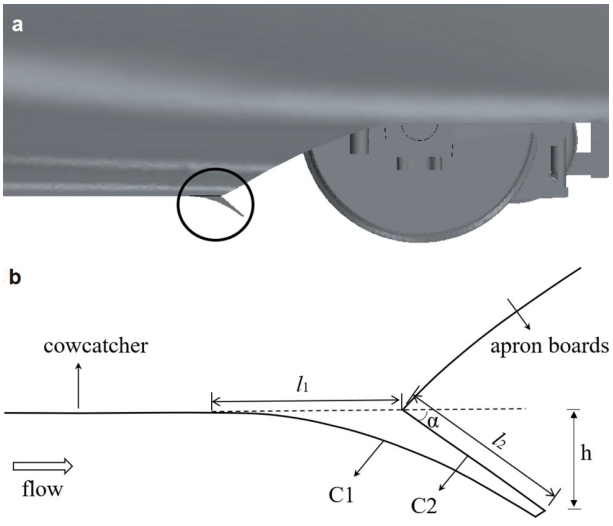

Figure 2 Schematic of the designed bottom deflector. **a** Mounting location; **b** detailed geometry.

Table 1 Simulation cases with different bottom deflector installation locations

	Train model	Deflector number	Deflector locations
Case 1	Prototype model	0	–
Case 2	Modified model	12	D1-D12
Case 3	Front-mounted model	6	D1, D3, D5, D7, D9, D11
Case 4	First-mounted model	1	D1

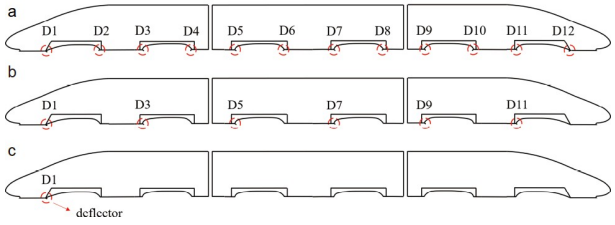

Figure 3 Three train models mounted with bottom deflectors in different locations: **a** modified train model, **b** front-mounted train model, and **c** first-mounted train model.

bogie cabins of the CRH380A train model, as shown in Fig. 3a; the front-mounted train model has mounted six bottom deflectors only before the six bogie cabins of the train, as shown in Fig. 3b; finally, the first-mounted train model is mounted with only one bottom deflector before the first bogie cabin of the train, as shown in Fig. 3c.

3. Computational details

3.1 Computational domain and boundary conditions

As depicted in Fig. 4, the computational domain extends 22.7H in the front of the train and 46.4H behind the train. The top of the computational domain is at a distance of 12H from the bottom of the rails, and the both sides are at a distance of 8.57H from the center of the train. The same computational domain is used in the simulations of all train models in this paper.

The corresponding Mach number of the train speed (350 km/h) is 0.286, and hence the flow is near the compressible regime. As a result, the inlet, outlet, and far-field of the computational domain are all set as the non-reflective free-flow boundary conditions. Moreover, the no-slip wall condition is used on the train surface to determine the friction and pressure on the surface. The ground is set as the moving no-slip wall boundary condition with the same speed as the train (but in the opposite direction) to simulate the ground effect caused by the relative motion between the train and the ground.

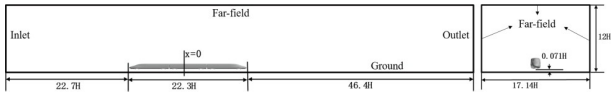

Figure 4 Computational domain.

3.2 Meshing strategy

In this study, the trimmed hexahedral grids are used in the outward zone of the train, while prism layers are employed in the near-wall area. The standard wall function, which models the wall effects directly to the logarithmic sub-layer of a turbulence boundary layer, is used to solve the near-wall turbulence to reduce the computational cost of unsteady simulations of full-scale high-speed trains. A similar mesh strategy was also adopted by many other researchers, such as Zhang et al. [21], Yao et al. [25], Muld et al. [26], and Guo et al. [27], and had been validated in their researches. Specifically, ten prism layers are used near the wall surface, and the height of the first prism layer is set as $2.29 \times 10^{-4}H$ to meet the y+ requirement ($30 < y+ < 150$) of the application of the standard wall function [28]. To better connect with the outer trimmed hexahedral grids and ensure good quality of grids, the growth rate of the prism layers is set to 1.2-1.5. The height of the boundary-layer grids, the orthogonality and the body-fitted characteristic between the boundary-layer grids and the train surface ensure the accuracy of the standard wall function in the boundary layer simulation. Moreover, to accurately capture the details of the flow structures around the high-speed train, the grids are both densified near the bogies and inter-carriage gaps, and the maximum grid size in these zones is limited to $9.14 \times 10^{-3}H$. In addition, the trimmed hexahedral grids are also refined to create three blocks around the train and the wake zone, and the minimum and maximum grid sizes in these zones are limited to $1.83\times10^{-2}H$ and 0.146H, respectively. The detailed layout of the grids on the cross-section of $y = 0$ is shown in Fig. 5. As a result, totally about 40 million grid cells are generated in the computational zone. Notably, the above grid parameters had been successfully verified by grid convergence tests for the same CRH380A high-speed train model in the authors' previous study [20].

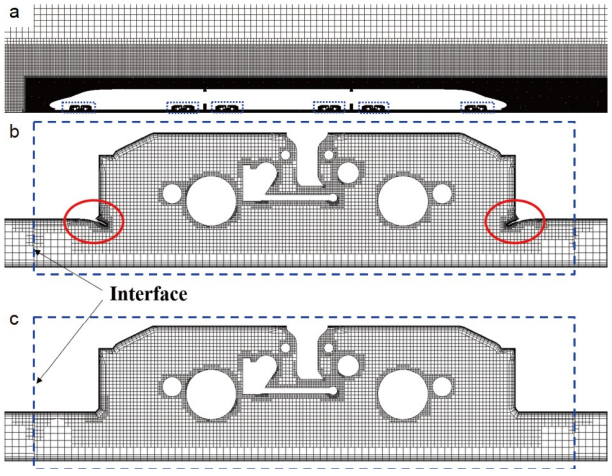

Figure 5 Grid layout on the cross-section of $y = 0$. **a** The whole train; **b** a bogie zone with deflectors; **c** a bogie zone without deflectors.

Traditionally, all the volume grids around the whole train need to be regenerated when the bottom deflectors are mounted on the train or their installation locations are changed. An interface method is introduced and applied to the bogie zones to exclude the influence of the change of grids around train except the zone near the bogies in comparison analyses between different train models. Here, interface is one kind of internal boundary, which separates the flow region into two or more sub-regions in the aspect of meshing and is compatible of different grid distributions on both sides. This allows that the grids in different sub-regions can be generated separately with different meshing strategies. Notably, the flows in different sub-regions separated by interfaces connect to each other physically. Hence, flow information pertaining to different sub-regions needs to be exchanged through these interfaces with an interpolation method during numerical simulations. In addition, to reduce error during the interpolation process, the grid sizes near both sides of an interface are required to match each other. As indicated by the blue dotted boxes in Fig. 5a, six zones are dug out around the six bogies, and each zone represents one bogie zone. All these bogie zones are donated as Region 2, while the remainder is Region 1. When the bottom deflectors are added to the train model or their installation locations are changed, only the grids in Region 2 need to be changed and regenerated at different cases, while the grids in Region 1 remain unchanged. The grids near the interface with and without the bottom deflectors are shown in Fig. 5b and c, respectively.

3.3 Numerical methods

Although numerical simulation methods in engineering applications are rather mature, difficulties still exist regarding the simulation of the real flow field of the high-speed train with complex geometry and large size. It is difficult to balance the computational cost and the accuracy of the simulation results. The IDDES method has unique advantages in solving strong separation flows with high Reynolds numbers. It behaves as a RANS (Reynolds-Averaged Navier-Stokes equations) model close to the walls to resolve the small-scale pulsation with less calculation cost and as a LES (Large Eddy Simulation) model in regions away from the walls to resolve the motion of the large separation vortices with high accuracy. Additionally, the IDDES method can also improve the unphysical separation caused by stress loss of models and grids [5,19,23,29-32].

The shear stress transport (SST) k-ω turbulence model is chosen to close the turbulent compressible Navier-Stokes (N-S) equations in the IDDES method in this study. Moreover, the dual time-stepping technique that introduces inner iteration in pseudo-time is also employed. The physical time-step is set as 5×10^{-4} s with at least 10 inner iterations to ensure that the residual value drops by at least two orders of magnitude in each physical time step. With detailed convergence verification, the Courant-Friedrichs-Lewy (CFL) number of inner iterations setting as 5 meets the requirement of calculation accuracy. All the above methods are implemented within the STAR-CCM+ commercial software [28].

4. Numerical validation

Since grid convergence had been successfully verified to the same high-speed train model in the authors' previous study and the simulation results were also in good agreement with those of wind tunnel experiments [20], numerical validation in this section focuses on the effectiveness of the application of the interface method. Two sets of computational grids for the original CRH380A high-speed train model (the prototype train model) are generated, namely the directly generated grids without interfaces (denoted as DM) and the grids with the use of interfaces (denoted as IM, Fig. 5c). Unsteady simulations are carried out, and the aerodynamic forces are evaluated and compared between these two meshing methods. In the later discussions, C_d is the drag coefficient defined as

$$C_d = \frac{F_d}{0.5\rho U_\infty^2 S},$$

where F_d is the drag force, ρ the air density, and S the reference area. In this study, the reference area is chosen as the train's cross-sectional area and $S = 11.123$ m^2. Accordingly, the lift coefficient C_l and the side force coefficient C_s are defined in the same way.

Figure 6 shows the time history curves of C_d of each car. It can be revealed that the flow field has been fully developed, and the aerodynamic drag coefficients of each car only fluctuate around their mean values after the physical time exceeding 1.5 s. Thereafter, the aerodynamic drag coefficients can be evaluated through their time averages, and all results are summarized in Table 2. For comparison, the

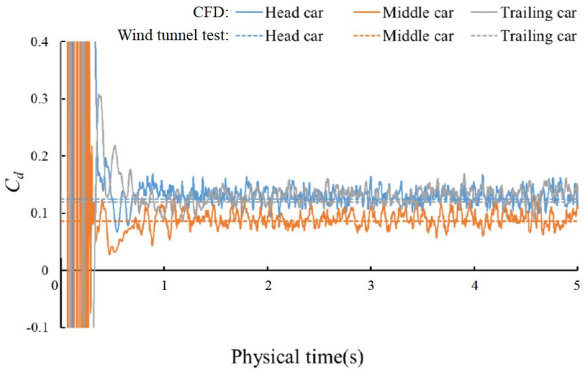

Figure 6 Comparisons of time history curves of C_d of each car between CFD and wind tunnel test.

Table 2 Comparisons of C_d obtained by different meshing methods

Meshing method	Head car	Middle car	Trailing car	Total	Difference
DM	0.1322	0.0888	0.1338	0.3548	–
IM	0.1286	0.0914	0.1352	0.3552	0.11%

corresponding wind tunnel test results [33] of a 1/8th scaled train model, conducted at China Aerodynamics Research and Development Center (CARDC) in Sichuan, are also presented in Fig. 6 as the dashed lines. As seen, the aerodynamic drag coefficients of each car obtained by numerical simulations are in agreement with the wind tunnel test results.

As indicated in Table 2, the difference of C_d obtained by the DM and IM is smaller than 0.2%. Moreover, to intuitively compare the differences of C_d simulated by these two meshes, the train is divided into 390 slices along its length direction (streamwise direction), resulting in a length of 0.2 m for each slice. Then, the time-averaged aerodynamic drag is integrated into each slice to obtain the sliced drag coefficient. Finally, the distributions of the time-averaged drag coefficient of these slices using different meshing methods are shown in Fig. 7. By comparing the distributions of C_d between these two meshes, it can be revealed that they almost overlap with each other, which implies that the interface method is capable of capturing the aerodynamic forces of high-speed trains and is suitable to the comparison of aerodynamic drag between different cases in this paper.

5. Results and discussion

5.1 Effectiveness of bottom deflectors

5.1.1 Aerodynamic forces

This section mainly discusses the effects of the added bottom deflectors on aerodynamic drag reduction of high-speed trains. The bottom deflectors (indicated by the twelve red circles) mounted on the bogie zone of the modified train model are shown in Fig. 3a. Six pairs of deflectors are installed near the six bogies, and each pair of deflectors are installed symmetrically in the front and rear ends of the bogie cabin to meet the two-way running condition of the train,

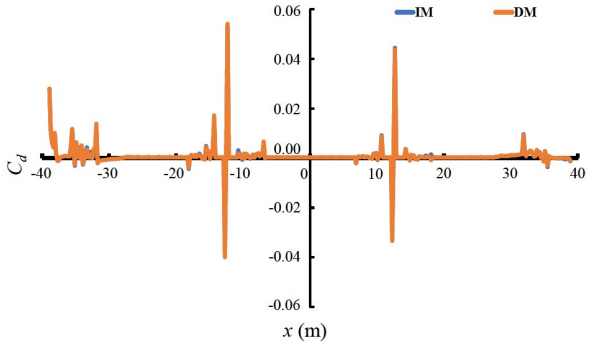

Figure 7 Distributions of C_d of slices obtained by different meshing methods.

resulting in totally 12 deflectors mounted in the modified train model. The calculated drag coefficients of the high-speed trains with 12 bottom deflectors are summarized in Table 3. For comparison, results of the prototype train model without any deflectors are given as well. It can be revealed that compared with the prototype train model, the drag coefficient of the head car of the modified train model significantly decreases, and it slightly decreases for the middle car. On the contrary, the drag coefficient of the trailing car increases with the installation of bottom deflectors. Nevertheless, the total drag coefficient of the modified train model with bottom deflectors decreases by 7.15%, which is a considerably large drag reduction effect.

To further analyze the effects of bottom deflectors on aerodynamic drag reduction, the drag coefficients of the trains are subdivided into different parts, such as bogie zones, bogie cabins, and bogies themselves, also summarized in Table 3. Notably, each bogie zone comprises a bogie cabin and a bogie, as indicated in Fig. 5. There are six bogies in the present train models, and they are numbered as 1 to 6 in sequence from the front to the tail for discussion simplicity. As depicted in Table 3, the total aerodynamic drag coefficient of the six bogie zones of the prototype train model is 0.2071, about 58.3% of the total aerodynamic drag (0.3552) of the train, which arises the facts that bogies contribute a large amount of aerodynamic drag to a high-speed train and that it is imperative to optimate the flow under the train to reduce the aerodynamic drag. By adding the bottom deflectors, the drags in the first three bogie zones (Zones 1-3) of the modified train model all reduce compared with the prototype train model, and the drag reduction effects gradually decrease from Zone 1 to Zone 3. On the contrary, the drags in the last three zones (Zones 4-6) of the modified train model increase to a similar extent. Furthermore, as for the aerodynamic drags that acted on the bogies of the prototype train model without any bottom deflectors, Bogie 1 suffers the greatest aerodynamic drag, while the Bogie 2 takes the second place, etc. However, when the bottom deflectors are added to the modified train model, all the aerodynamic drags of these six bogies significantly decrease, all with a change from positive values to negative values, implying that pushing forces are performed on these bogies. Among these bogies, the aerodynamic drag of Bogie 1 changes greatly, from the largest drag to the largest pushing force.

To compare the aerodynamic drag distributions of the high-speed trains with or without the bottom deflectors in a more intuitive way, the whole train is again sliced as in Sect. 4, and the time-averaged drag coefficient of each train slice is counted and shown in Fig. 8. The detailed slicing method is the same as that used in Fig. 7. The blue line represents the distribution of slice drags of the prototype train model, while the orange line represents that of the modified train model. It can be clearly seen that the existence of the bottom deflectors

Table 3 Drag coefficients of high-speed trains with or without bottom deflectors[a)]

Train model	Head car	Middle car	Trailing car	Total	Difference		
Prototype model	0.1286	0.0914	0.1352	0.3552	–		
Modified model	0.0864	0.0904	0.1530	0.3298	−7.15 %		
	Zone 1	Zone 2	Zone 3	Zone 4	Zone 5	Zone 6	Sum
Prototype model	0.0836	0.0294	0.0241	0.0200	0.0192	0.0308	0.2071
Modified model	0.0571	0.0228	0.0203	0.0269	0.0239	0.0351	0.1861
	Cabin 1	Cabin 2	Cabin 3	Cabin 4	Cabin 5	Cabin 6	Sum
Prototype model	0.0500	0.0191	0.0155	0.0135	0.0133	0.0210	0.1324
Modified model	0.0626	0.0239	0.0222	0.0276	0.0248	0.0356	0.1967
	Bogie 1	Bogie 2	Bogie 3	Bogie 4	Bogie 5	Bogie 6	Sum
Prototype model	0.0336	0.0103	0.0086	0.0065	0.0059	0.0098	0.0747
Modified model	−0.0055	−0.0011	−0.0019	−0.0007	−0.0009	−0.0005	−0.0106

a) The drag coefficients satisfy the following relation: $C_{d,\,\mathrm{zone}} = C_{d,\,\mathrm{cabin}} + C_{d,\,\mathrm{bogie}}$.

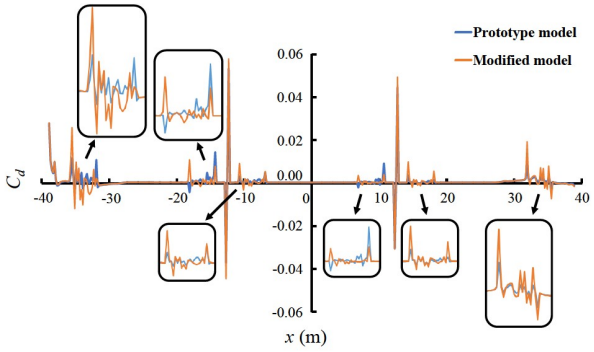

Figure 8 Drag coefficients of slices of the prototype and modified train models.

has a large effect on the drag distribution near the bogie zones. With the bottom deflectors mounted near the bogies, the front-side (near the head car) of the bogie zone bears more drag, since the bottom deflector deflects the incoming airflow and bears some extent of the impact of the flow in the meanwhile. On the contrary, the drag of the rear-side plate of the bogie cabin is otherwise smaller since the deflector blocks the incoming flow. Compared with the drag distribution of the prototype train model, this local induced drag in the modified train model can be thought to be transferred from the rear-side to the front-side in the bogie zone; that is, from the rear-side plate of the bogie cabin to the windward side of the deflector. As a result, the drags of the bogie cabins would not extensively increase with the bottom deflectors mounted, with the total aerodynamic drag of the bogie cabins (including the deflectors) changing from 0.1324 to 0.1967, as shown in Table 3. However, the total aerodynamic drag coefficient of the bogies decreases significantly from 0.0747 to −0.0106 with the bottom deflectors installed, leading to the final large reduction of total drag to the train (from 0.3552 to 0.3298, with a relative reduction percentage of 7.15%). That is to say, the effect of the bottom deflectors on drag reduction mainly origins from the bogies.

In addition, Table 4 summarizes the time-averaged lift coefficients of different high-speed train models with or without bottom deflectors. For a traditional high-speed train (i.e., the prototype train model in this paper), the head car always suffers from the largest negative lift, while a large positive lift is presented in the trailing car. The lift of the middle car is nearly zero. From the aspects of engineering practices, the aerodynamic lift is expected to be positive to compensate for the large gravity load to reduce wheel/rail wear and tear, but it is also expected to be not very large for operation safety, especially the trailing car. Compared with the prototype train model, the aerodynamic lifts of the head car and middle car of the modified train model, with the bottom deflectors mounted near the bogies, slightly increase by 0.0048 and 0.0109, respectively. Most importantly, the aerodynamic lift of the trailing car of the modified train model decreases significantly from the large positive value of the prototype train model to a near-zero value. In other words, the mounting of bottom deflectors not only reduces the aerodynamic drags but also helps to improve the aerodynamic lift performance of high-speed trains.

Since the unsteady characteristics of the aerodynamic forces acting on the train are important to its operation safety, the changes of these unsteady characteristics after using bottom deflectors need to be checked as well. Table 5 compares the standard deviations of the fluctuating aerodynamic forces of each car between the prototype train model without bottom deflectors and the modified train model with bottom deflectors. It can be revealed that the existence of bottom deflectors increases the standard deviations of aerodynamic forces of all three cars. Fortunately, these increasements are not in order of magnitude (the maximum change in unsteady aerodynamic characteristics is within 1.5 times of the original ones). This means that although the bottom deflectors worsen the aerodynamic performance in the aspect of unsteady characteristics, they still bear a large application potential due to their excellent improvements in time-averaged aerodynamic drags and lifts,

Table 4 Lift coefficients of high-speed trains with or without bottom deflectors

Train model	Head car	Middle car	Trailing car
Prototype model	−0.0553	−0.0084	0.0301
Modified model	−0.0505	0.0025	0.0056
Absolute difference	0.0048	0.0109	−0.0245

Table 5 Standard deviations of aerodynamic forces of each car of the two high-speed train models

Aerodynamic coefficient	Train model	Head car	Middle car	Trailing car
C_d	Prototype model	1.24×10^{-2}	1.42×10^{-2}	1.29×10^{-2}
	Modified model	1.67×10^{-2}	1.52×10^{-2}	1.80×10^{-2}
	Difference	34.68%	7.04%	39.53%
C_l	Prototype model	2.90×10^{-2}	3.35×10^{-2}	3.13×10^{-2}
	Modified model	3.43×10^{-2}	3.63×10^{-2}	3.59×10^{-2}
	Difference	18.28%	8.36%	14.70%
C_s	Prototype model	1.28×10^{-2}	1.67×10^{-2}	1.96×10^{-2}
	Modified model	1.37×10^{-2}	2.03×10^{-2}	2.76×10^{-2}
	Difference	7.03%	21.56%	40.82%

and that further optimizations would be required to improve the unsteady aerodynamic performance of the bottom deflectors in the future.

5.1.2 *Flow field structures*

Figure 9 depicts the time-averaged surface pressure distributions of the prototype and modified train models. It can be revealed that the pressure distributions of these two models are almost the same as the top view, but they are rather different at the bottom of these trains, especially on the deflectors, bogies, and bogie cabins; that is, the presence of the bottom deflectors has little effect on the upper part of the train but affects the underbody flow of the train greatly, especially in the bogie zones.

A more detailed and clear comparison of the pressure distribution in the bogie zones between these two train models can refer to Fig. 10. As seen, the windward sides of the bogies and the bogie cabins of the prototype train model, without any deflectors, are subjected to strong positive pressure, especially in the first bogie zone where the pressure differential effect is rather obvious. This pressure differential effect causing severe aerodynamic drag becomes smaller and smaller for the backward bogies. The corresponding pressure distributions change distinctly with the bottom deflectors mounted in the bogie zones. The positive pressure is concentrated on the windward sides of the deflectors, and almost no obvious pressure differences occur on the bogies and bogie cabins, resulting in a uniform distribution of pressure after each deflector. Overall, the pressure level in the bogie zones of the modified train model is lower than that of the prototype train model.

Since the deflectors have the largest effects on the first two bogie zones, the time-averaged velocity distributions on the plane of $y = 0$ of head car of the prototype and modified train models are shown in Fig. 11. It can be seen that the velocity distributions at the bottom of these two train models are significantly different. As for the prototype train model without any deflectors mounted, the flow velocity near the rail guard would increase suddenly due to the sharp reduction of cross-section the bottom space when the air flows through the train. This high-speed underbody flow would directly impact the bogies and other bottom equipment due to their exposure under the train body, leading to large aerodynamic drags. As for the modified train model with deflectors mounted, the high-speed underbody flow would be blocked and induced to the ground rather than impinging on the bogies when it passes through the windward side of the deflectors. This induced airflow just like a jet flow, and it would also take away part of the air in the bogie cabin when it rushes to the ground, reducing pressure in the bogie cabin, which agrees with the results shown in Fig. 10. Thereafter, the velocity of the underbody flow near the train floor decreases accordingly, which not only benefits reducing the

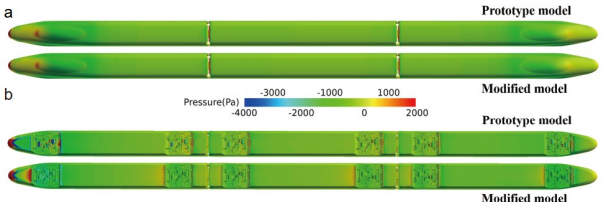

Figure 9 Time-averaged pressure distributions of different train models. **a** Top view; **b** bottom view.

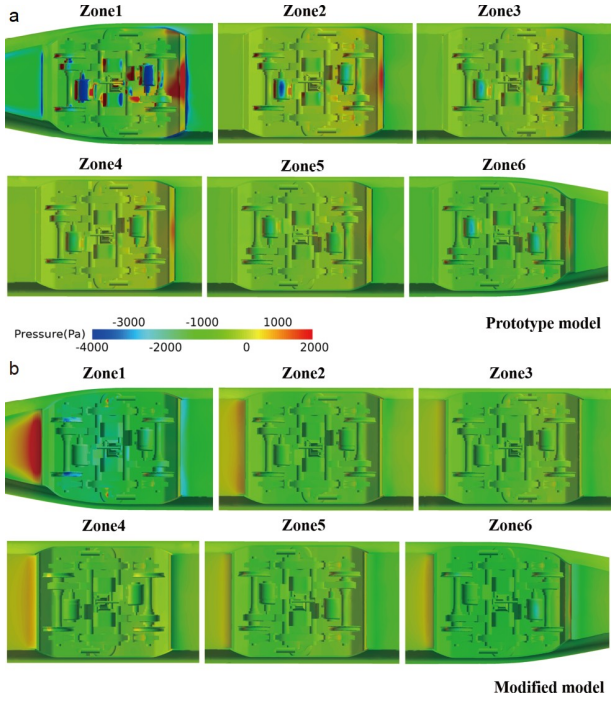

Figure 10 Time-averaged pressure distributions of bogie zones of different train models.

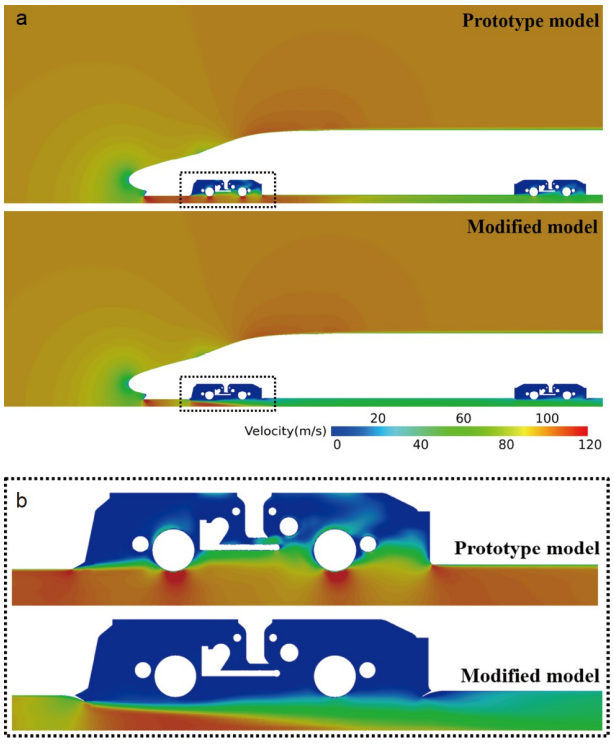

Figure 11 Time-averaged velocity distributions on the plane of $y = 0$: **a** head car, **b** zone 1.

friction drags at the bottom of the train body but also weakens the impinging effects of the underbody flow bottom equipment of latter carriages.

Further, Fig. 12 depicts the results of the time-averaged velocity component u along the length-direction (x-direction) of the train, on the line of (y, z) = (0, 0.1) m. Obviously, the velocity of the underbody flow of the modified train model is significantly lower than that of the prototype train model, especially in the first bogie zone where the u-component decreases sharply after the flow passes through the first deflector. Since the selected line is slightly higher than the bottom end of the first deflector in the z-direction (the first deflector is mounted on the cowcatcher that is 0.05 m lower than the train bottom), the negative value of u is caused by the leeside-effects of the first deflector. After the first deflector, the decrease of u of the modified train model is weaker and weaker. However, a significant deceleration phenomenon of the underbody flow still occurs in the later bogie zones.

5.1.3 *Velocity and pressure profiles within the bogie zones*

Figure 13a shows the location of six pairs of extraction lines (i.e., twelve lines, numbered as 1-12 orderly) in the bogie zones at the symmetric plane ($y = 0$). The two lines of one pair are symmetrically spaced $0.94H$ with each other. The profiles of the time-averaged streamwise velocity component (u) along these twelve lines are presented in Fig. 14.

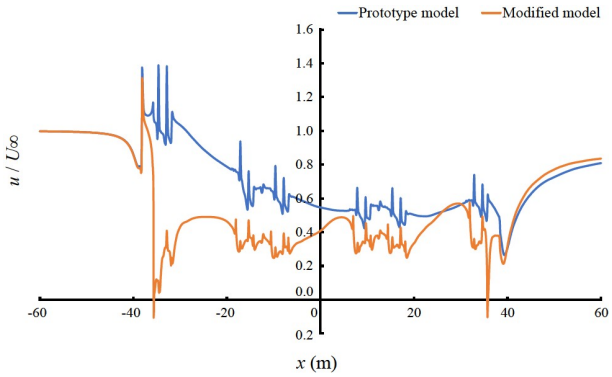

Figure 12 Time-averaged distributions of velocity component u of different train models, along the line of (y, z) = (0, 0.1) m.

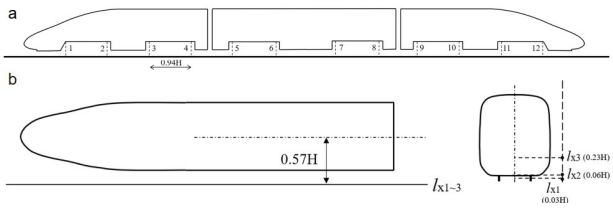

Figure 13 Schematic of locations of the extracted lines. **a** Lines 1-12; **b** l_{x1}-l_{x3}.

Overall, the velocity level of the airflow decreases along the train's length, which is similar to that reported by Zhang et al. [21] and Xia et al. [34]. When the comparison is conducted between different train models, it can be seen that the u-component velocity along the lines (Lines 2, 4, 6, 8, 10, and 12) on the windward sides of the bogie cabins of the modified train model is significantly lower than that of the prototype train model, especially along Line 2. This velocity difference becomes lower and lower along the train's length backward, implying that the effectiveness of the bottom deflector on blocking airflow is weaker and weaker. The largest effect of the deflectors is concentrated on the head car, more precisely, in the first bogie zone. Moreover, the differences of u-component velocity along the lines (Lines 1, 3, 5, 7, 9, and 11) on the leeward sides of the bogie cabins between the prototype and modified train models are also very significant and mainly occur in the zones under the floor of the train body. With the bottom deflectors mounted in the bogie zones, the position of the maximum velocity gradient has a significant downward shift. Additionally, the u-component velocity of the underbody flow of the first half of the modified train model (Lines 1, 3, and 5) decreases significantly compared with the prototype train model, while that of the second half of the modified train model (Lines 7, 9, and 11) increases or decreases with only little differences.

To further analyze the drag reduction effect of the bottom deflectors, the distributions of the pressure difference between the two lines of each pair in each bogie zone are evaluated by subtracting the leeward pressure from the

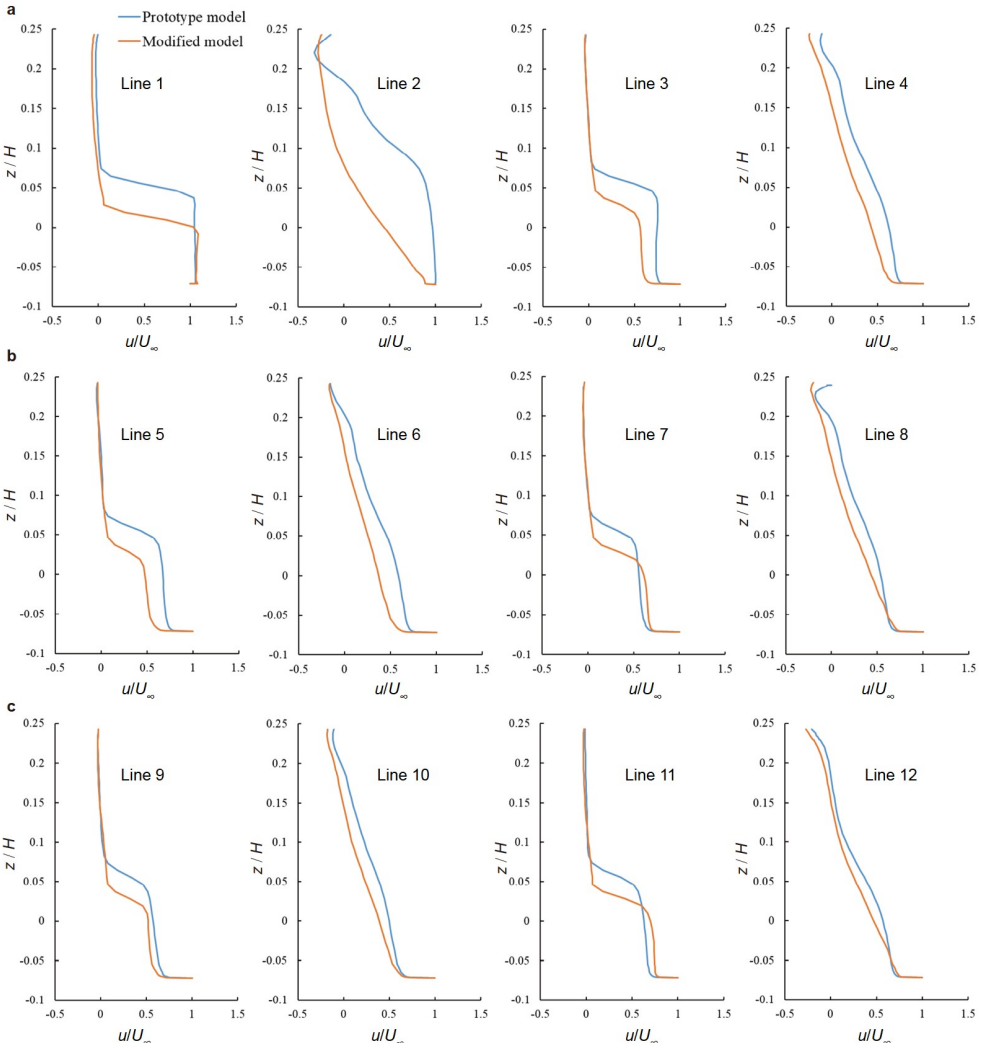

Figure 14 Time-averaged distributions of velocity component u along different lines in the bogie cabins.

windward pressure and shown in Fig. 15. As seen, the pressure differences of the modified train model are overall smaller than those of the prototype train model, and even negative pressure differences exist in the modified train model. These results further demonstrate the effectiveness of the deflectors in drag reduction in the bogie cabins (excluding the deflectors). The pressure difference in the bogie zone is reduced by reducing the pressure on the windward side to avoid a large pressure drag in this part.

Furthermore, distributions of time-averaged u-component velocity along Lines l_{x1}, l_{x2}, and l_{x3} are given in Fig. 16, presenting a large difference of u between these two train models as well. The locations of Lines l_{x1}, l_{x2}, and l_{x3} are also shown in Fig. 13b. Line l_{x1} lies at the half-height from the train floor to the top of rails, while Line l_{x2} is at the same height as the train floor. Line l_{x3} is about $0.23H$ away from the top of rails in height. These three lines are $0.57H$ away from the center of rails in the spanwise direction. As indicated in Fig. 16, after passing through the first bogie, the underbody flow of the modified train model has a greater u than the prototype train model, and this difference in u gradually decreases until the wake. Moreover, although the u-component of the modified train model is relatively larger, its value is closer to the train speed of U_∞. Generally, as for an incoming flow with a speed of U_∞, the existence of a train would reduce the flow speed, especially around the train floor where bottom equipment is exposed. Therefore, the influence of the modified train model on the incoming flow is smaller than that of the prototype train model. The smaller influence of the train to the incoming flow, the smaller influence of the flow to the train accordingly, which further explains why the modified train model with bottom deflectors has less drag than the prototype train model. Further, by comparing the results of Lines l_{x1}, l_{x2}, and l_{x3}, it is found that the velocity curves of these two train models gradually overlap with the increase of height, implying that bottom deflectors have little effect on the upper part of the train, and they only affect the underbody flow of the train greatly, especially in the bogie zones.

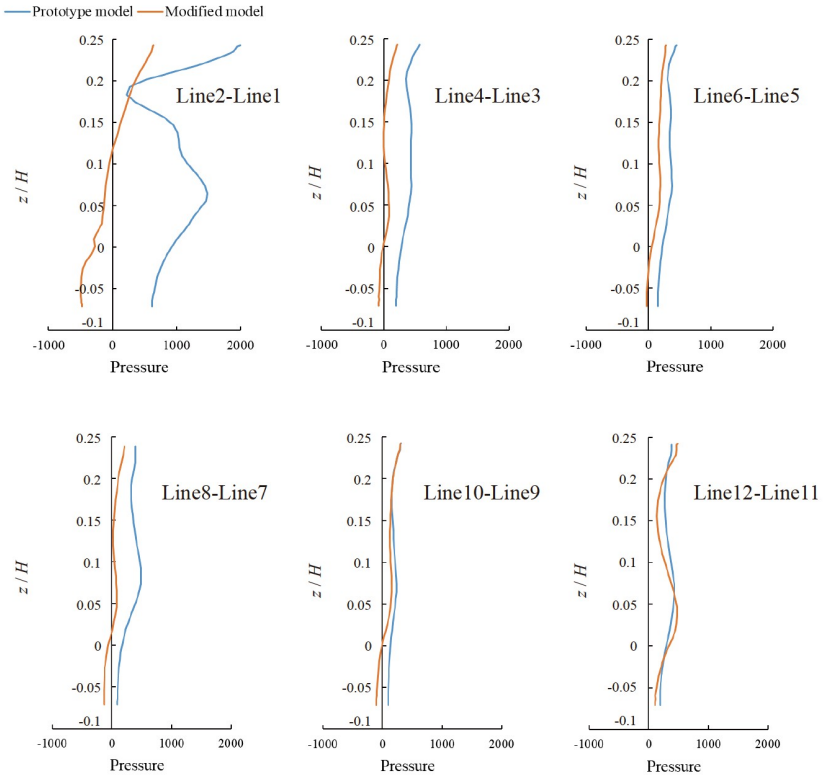

Figure 15 Profiles of pressure difference between each pair of lines.

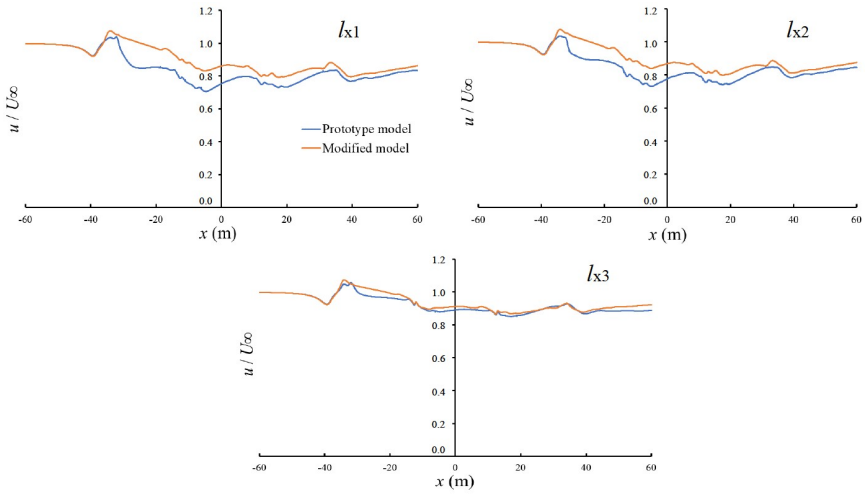

Figure 16 Time-averaged distributions of u along lines l_{x1}, l_{x2}, and l_{x3}.

5.2 Effects of the mounting location of deflectors

5.2.1 Optimal mounting locations in drag reduction

This section mainly analyzes the effects of different installation locations of the bottom deflectors on drag reduction of the train. The reversed placed deflector is lower than the train floor in height, so it may contribute extra aerodynamic drag to the train by catching the incoming flow. Therefore, the third train model named the front-mounted train model that only installs deflectors on the front ends of the bogie cabins is designed and simulated, as shown in Fig. 3b; that is, totally only six bottom deflectors (D1, D3, D5, D7, D9, D11) are mounted on the front-mounted train model, compared with the twelve bottom deflectors mounted on the modified train model previously.

Figure 17 depicts the streamlines near the rear end of the first bogie zone of the modified train model and the front-mounted train model, with time-averaged pressure distributions given by color contours. It can be found that the in-

coming flow impacts on the windward side of the reversed placed deflector in the modified train model, resulting in a vortex with increased pressure on the windward sides of the bogie cabin and the deflector and a low-pressure vortex on the leeward side of the reversed placed deflector. Consequently, extra pressure drag is induced by the reversed placed deflector in the modified train model. By removing all the reversed placed deflectors in the front-mounted train model, a vortex still forms near the windward side of the bogie cabin, but its strength and size reduce significantly. Most of the incoming airflow flows downstream directly, and only a litter flows upward along with the rear plate of the bogie cabin. Hence, the pressure enforced on the rear plate is lower than that of the modified train model, which is conducive to reducing the pressure drag of the front-mounted train model.

As discussed in Sect. 5.1, the main drag reduction effect by mounting bottom deflectors occurs in the head car for the modified train model. The drag reduction of the middle car is very small, while the drag of the trailing car increases instead of decreasing. Additionally, the effectiveness of the bottom deflectors on blocking and defecting the incoming airflow is mainly concentrated in the first bogie zone. Therefore, the fourth train model named the first-mounted train model is designed and simulated as well, where only one deflector (D1) is mounted on the front end of the first bogie cabin of the head car, as shown in Fig. 3c.

The comparison of the aerodynamic drag coefficients of the above four train models is summarized in Table 6. Compared with the prototype train model, the drag coefficients of the head cars of the three designed train models are all significantly reduced, while those of the middle cars are only slightly reduced. The main difference between these train models is that the drag coefficients of the trailing cars of the modified train model and the front-mounted train model greatly increase, whereas it only slightly changes for the first-mounted train model. Moreover, compared with the modified train model, the aerodynamic drag of each car of the front-mounted train model decreases by removing the reversed placed deflectors. Finally, a total drag reduction of 11.48% of the front-mounted train model compared with the prototype model is achieved. As for the first-mounted train model, it is found that although the drags of the head car and middle car increase slightly compared with the front-mounted train model, the drag of the trailing car decreases significantly and is similar to that of the prototype train model. Finally, a total of 11.99% drag reduction of the first-mounted train model is achieved, compared with the prototype train model. From all above, the optimal mounting configuration is only mounting one bottom deflector on the front end of the first bogie zone (i.e., the first-mounted train model).

5.2.2 *Slipstream*

After determination of the optimal mounting configuration of the bottom deflectors by comparing the drag reduction effects of different train models, the extra effects of the mounted deflector of the optimal train model (i.e., the first-mounted train model) on slipstream, compared with the prototype train model, are discussed in this section, since the slipstream induced by lower part of the train is commonly more obvious. Figure 18 depicts the comparison of boundary layer, estimated by a velocity value of $0.99U_\infty$, between the prototype and first-mounted train models. Note that these boundary layer profiles are taken at the middle of each car along the length direction. On the whole, the boundary layer thicknesses of these two train models, near the train body of each car, are basically the same. The boundary layer thickness increases along the train's length in a consistent way whether the first deflector is mounted or not. As a result, the boundary layer thickness of the head car is smaller than the downstream ones, and the thickness of the trailing car is the largest.

Table 6 Comparison of drag coefficients between the four train models

Train model	Head car	Middle car	Trailing car	Total	Difference
Prototype model	0.1286	0.0914	0.1352	0.3552	–
Modified model	0.0864	0.0904	0.1530	0.3298	−7.15%
Front-mounted model	0.0766	0.0861	0.1517	0.3144	−11.48%
First-mounted model	0.0850	0.0899	0.1377	0.3126	−11.99%

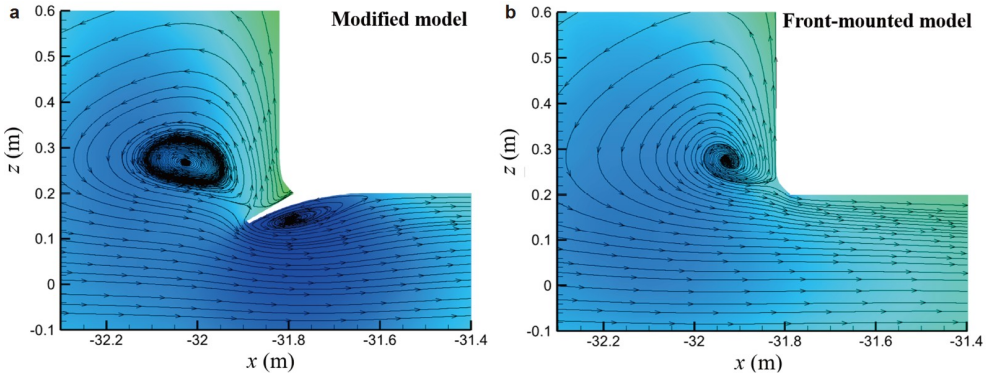

Figure 17 **a** Streamlines of the modified train model and **b** the front-mounted train model near the rear end of the first bogie cabin.

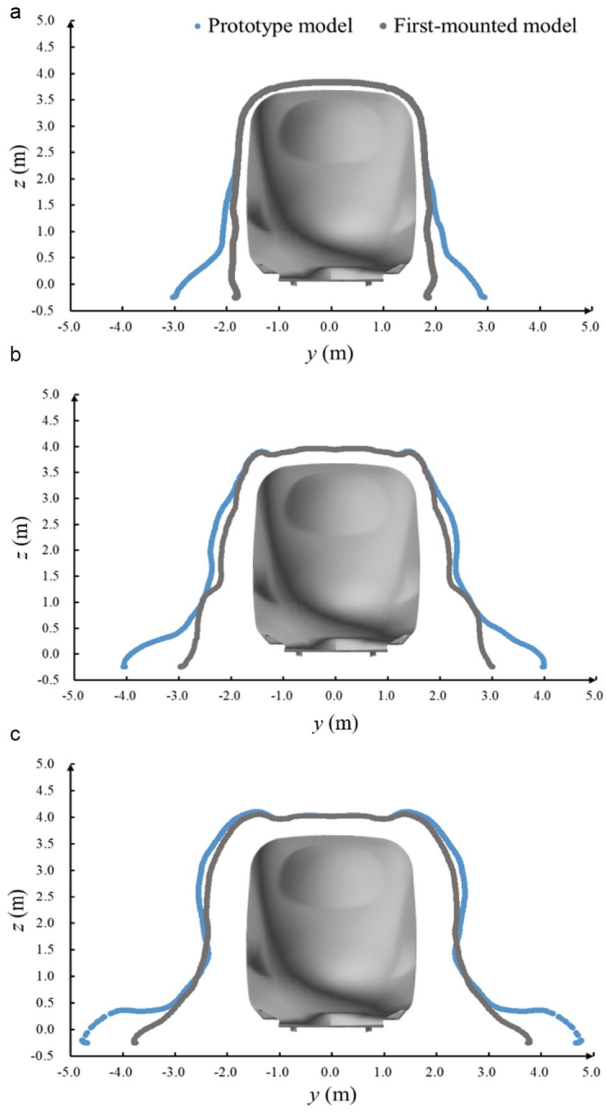

Figure 18 Comparisons of boundary layer locations between different train models, in the middle sections of different cars: **a** head car, **b** middle car, and **c** trailing car.

However, the main difference in the boundary layer between these two train models appears near the bottom of the train. The isolines of velocity at the top and both sides of these two train models have a high degree of coincidence, while they are significantly closer to the bottom of the train body for the first-mounted model. The lower in height, the greater the difference in boundary layer is, and the greatest difference occurs at the ground. Generally speaking, the location of $0.99U_\infty$ isoline near the ground represents the influence range of the bottom of the train and the bottom devices on the underbody flow field. That is to say, the closer the isolines are to the train body, the smaller the influence range of the train is. Therefore, the spanwise influence range of the first-mounted train model is reduced by about one meter compared with the prototype train model, indicating that the presence of the bottom deflector significantly reduces the interference effect of the bottom of the train and bottom devices on the underbody flow.

The comparison of the time-averaged slipstreams (U_w) between these two train models is shown in Fig. 19. The slipstreams are given along two horizontal lines of (y, z) = (3, 0.2) m and (3, 1.4) m, respectively. Notably, the line of (y, z) = (3, 0.2) m is at the same height of the bottom of the train body and is greatly influenced by the underbody flow and ground effect, while the line of (y, z) = (3, 1.4) m is at about half of the train's height and is also at the same height level of a human body, where the train slipstream is important to human safety. In the following, the slipstreams in three different but representative regions discussed by Baker [35], namely the nose region, the boundary-layer region and the wake region, are detailly analyzed.

In the nose region at z = 0.2 m or z = 1.4 m, there is a small increase in the time-averaged slipstream of the first-mounted train model compared with the prototype train model, which is possibly attributed to the fact that the bottom deflector not only guides the underbody airflow to the ground but also guides a little amount of flow to both sides of the train at the same time because of its quasi-two-dimensional geometry. In the boundary-layer region, the level of slipstream basically depends on the thickness of boundary layer. As a result, the slipstream of the prototype train model grows significantly faster than that of the first-mounted train model at z = 0.2 m, as shown in Fig. 19a. This can be contributed to the faster growth of the bottom boundary layer thickness of the prototype train model, as indicated in Fig. 18. Moreover, the slipstreams of the two train models are almost at the same level at z = 1.4 m (Fig. 19b), which is then contributed to the

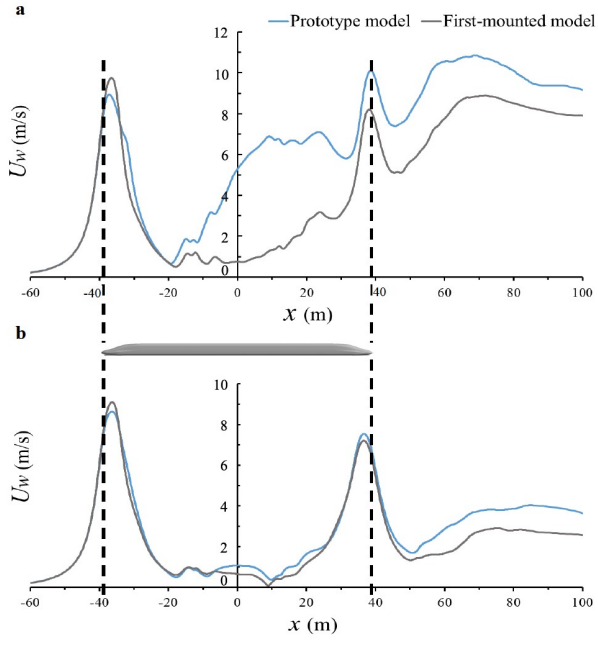

Figure 19 Time-averaged slipstreams along different train models at **a** (y, z) = (3, 0.2) m and **b** (y, z) = (3, 1.4) m.

consistent boundary layer thickness of these two trains near the train body. In the wake region, the slipstream reaches its local maximum value for both two train models. Nevertheless, the slipstream of the first-mounted train model in this region is about 2 m/s smaller than that of the prototype train model at z = 0.2 m, while it is about 1 m/s smaller at z = 1.4 m. This can be contributed to the fact that the existence of the bottom deflector weakens the strong unsteady flow in the bogie zones, reduces its disturbance introduced into the surrounding flow field, and subsequently weakens the formation of vortex structures in the wake. Consequently, the mounting of a bottom deflector in the first bogie zone of a high-speed train not only significantly reduces the total aerodynamic drag, but also obviously reduces the train's slipstream, which is benefited to the safety of railway workers and passengers waiting on the platforms.

6. Conclusions

In this paper, one kind of small and simple device, the bottom deflector, is proposed to be mounted before and/or after the bogie cabins to reduce the aerodynamic drag of the high-speed trains. Taking the classical CRH380A high-speed train as an example, the flow fields of the prototype train model without any bottom deflectors and three other modified train models with bottom deflectors are numerically studied by the IDDES method combined with the interface method. Comparative analyses of the aerodynamic drags, pressure distributions and velocity distributions of these trains are conducted to demonstrate the effectiveness and further the mechanism of the bottom deflectors on aerodynamic drag reduction of the trains. It is suggested that the bottom deflectors can smoothly guide the underbody flow, which would hit on the bogies previously, to the ground and consequently reduce the aerodynamic drag of the train significantly. Moreover, the effects of different mounting locations of bottom deflectors on drag reduction are also analyzed. Results show that the optimal mounting configuration is to mount only one deflector on the front end of the first bogie zone of the train, and a maximum drag reduction percentage of 11.99% is finally achieved. Further, the mounted deflector is also proved capable of not only reducing the aerodynamic drag, but also significantly reducing the interference range of the underbody flow and reducing the slipstream of the train, which is benefited to the safety of railway workers and passengers waiting on the platforms.

Notably, although a high-speed train with 3 carriages is taken as an example in this paper, the effectiveness and mechanism of the bottom deflectors on drag reduction can be easily extended to other high-speed trains with more than 3 carriages. For example, as for a high-speed practice train with 8 or 16 carriages, a considerable drag reduction effect may be achieved by setting a bottom deflector every 3 carriages. In addition, considering the two-way running situation of high-speed trains, some small storage grooves can be easily designed under the train. The reversed placed deflectors can be withdrawn into the storage grooves when the high-speed train is running in the reverse direction. Note again that the effects of bottom deflectors on aerodynamic drag reduction and their relevant mechanisms are only discussed under an open-air operation condition of a high-speed train as an example, without considerations of other complex running conditions, such as crosswind and tunnel-crossing, which, however, would be served as the future work. Actually, the drag-reduction effects of bottom deflectors under these complex operation conditions may not deviate much from the open-air condition since the relevant flow control mechanism of these bottom deflectors does not change.

This work was supported by the National Key Research & Development Projects (Grant No. 2017YFB0202801), the Strategic Priority Research Program of the Chinese Academy of Sciences (class B) (Grant No. XDB22020000), and Research project of Chinese Academy of Sciences (Grant No. XXH13506-204).

1 R. S. Raghunathan, H. D. Kim, and T. Setoguchi, Aerodynamics of high-speed railway train, Prog. Aerosp. Sci. **38**, 469 (2002).
2 M. Yang, J. Du, Z. Li, S. Huang, and D. Zhou, Moving model test of high-speed train aerodynamic drag based on stagnation pressure measurements, Plos One **12**, e0169471 (2017).
3 S. S. Ding, Q. Li, A. Q. Tian, J. Du, and J. L. Liu, Aerodynamic design on high-speed trains, Acta Mech. Sin. **32**, 215 (2016).
4 T. Maeda, T. Matsumura, M. Iida, K. Nakatani, and K. Uchida, in Effect of shape of train nose on compression wave generated by train entering tunnel: Proceedings of the International Conference on Speedup Technology for Railway and Maglev Vehicles, Yokohama, 1993, pp. 315-319.
5 X. Li, G. Chen, D. Zhou, and Z. Chen, Impact of different nose lengths on flow-field structure around a high-speed train, Appl. Sci. **9**, 4573 (2019).
6 J. T. Du, A. Q. Tian, S. S. Nie, H. K. Li, and T. H. Liu, Research on the mapping relations between the drag and lift properties and the shape parameters of a high-speed train (in Chinese). J. Railw. Sci. Eng. **13**, 1017 (2016).
7 S. Yao, D. Guo, Z. Sun, G. Yang, and D. Chen, Optimization design for aerodynamic elements of high speed trains, Comput. Fluids **95**, 56 (2014).
8 G. Xu, X. Liang, S. Yao, D. Chen, and Z. Li, Multi-objective aerodynamic optimization of the streamlined shape of high-speed trains based on the Kriging model, Plos One **12**, e0170803 (2017).
9 L. Tian, L. Ren, Q. Liu, Z. Han, and X. Jiang, The mechanism of drag reduction around bodies of revolution using bionic non-smooth surfaces, J. Bionic. Eng. **4**, 109 (2007).
10 P. P. Sun, Research on aerodynamic drag reduction of high-speed train with non-smooth surface (in Chinese), Dissertation for the Master's Degree, (Zhejiang University, Hangzhou, 2012).
11 K. Tang, S. W. Ma, H. Q. Liang, and G. F. Ding, Simulation research of the drag reduction of high-speed train microstructured surfaces (in Chinese). Mach. Des&. Manuf. **9**, 213 (2020).
12 M. Y. Wang, S. A. Hashmi, Z. X. Sun, D. L. Guo, G. Vita, G. W. Yang, and H. Hemida, Effect of surface roughness on the aerodynamics of a high-speed train subjected to crosswinds, Acta Mech. Sin. **37**, 1090 (2021).

13 V. V. Pavlov, Dolphin skin as a natural anisotropic compliant wall, Bioinspir. Biomim. **1**, 31 (2006).
14 J. Wang, S. S. Koley, and J. Katz, On the interaction of a compliant wall with a turbulent boundary layer, J. Fluid Mech. **899**, A20 (2020).
15 E. O. Shkvar, A. Jamea, S. J. E, J. C. Cai, and A. S. Kryzhanovskyi, Effectiveness of blowing for improving the high-speed trains aerodynamics, Thermophys. Aeromech. **25**, 675 (2018).
16 R. Nolte, and F. Wurtenberger, Event evaluation of energy efficiency technologies for rolling stock and train operation of railways, International Union of Railways. Deutsche Bahn AG, Berlin, 2003.
17 M. Suzuki, K. Nakade, and A. Ido, Countermeasures for reducing unsteady aerodynamic force acting on high-speed train in tunnel by use of modifications of train shapes, JMTL **2**, 1 (2009).
18 G. Mancini, A. Malfatti, A. G. Violi, and G. Matschke, in Effects of experimental bogie fairings on the aerodynamic drag of the ETR 500 high speed train: Proceedings of the World Congress on Railway Research, Cologne, 2001.
19 J. Wang, G. Minelli, Y. Zhang, J. Zhang, S. Krajnović, and G. Gao, An improved delayed detached eddy simulation study of the bogie cavity length effects on the aerodynamic performance of a high-speed train, Proc. Institution Mech. Engineers Part C-J. Mech. Eng. Sci. **234**, 2386 (2020).
20 W. Liu, D. Guo, Z. Zhang, D. Chen, and G. Yang, Effects of bogies on the wake flow of a high-speed train, Appl. Sci. **9**, 759 (2019).
21 J. Zhang, J. Wang, Q. Wang, X. Xiong, and G. Gao, A study of the influence of bogie cut outs' angles on the aerodynamic performance of a high-speed train, J. Wind Eng. Industrial AeroDyn. **175**, 153 (2018).
22 G. J. Gao, Q. R. Chen, J. Zhang, Y. Zhang, Z. Tian, and J. Chen, Numerical study on the anti-snow performance of deflectors on a high-speed train bogie frame, J. Appl. Fluid Mech. **13**, 1377 (2020).
23 J. Niu, D. Zhou, and X. Liang, Numerical simulation of the effects of obstacle deflectors on the aerodynamic performance of stationary high-speed trains at two yaw angles, Proc. Inst. Mech. Eng. Part F-J. Rail Rapid Transit. **232**, 913 (2018).
24 Z. Guo, T. Liu, Z. Chen, Y. Xia, W. Li, and L. Li, Aerodynamic influences of bogie's geometric complexity on high-speed trains under crosswind, J. Wind Eng. Ind. Aerodyn. **196**, 104053 (2020).
25 S. B. Yao, Z. X. Sun, D. L. Guo, D. W. Chen, and G. W. Yang, Numerical study on wake characteristics of high-speed trains, Acta Mech. Sin. **29**, 811 (2013).
26 T. W. Muld, G. Efraimsson, and D. S. Henningson, Flow structures around a high-speed train extracted using proper orthogonal decomposition and dynamic mode decomposition, Comput. Fluids **57**, 87 (2012).
27 Z. Guo, T. Liu, H. Hemida, Z. Chen, and H. Liu, Numerical simulation of the aerodynamic characteristics of double unit train, Eng. Appl. Comput. Fluid Mech. **14**, 910 (2020).
28 STAR-CCM+ v9.06 User's Manual. CD-adapco Co., 2014.
29 S. Wang, J. R. Bell, D. Burton, A. H. Herbst, J. Sheridan, and M. C. Thompson, The performance of different turbulence models (URANS, SAS and DES) for predicting high-speed train slipstream, J. Wind Eng. Ind. Aerodyn. **165**, 46 (2017).
30 Z. X. Xiao, and K. Y. Luo, Improved delayed detached-eddy simulation of massive separation around triple cylinders, Acta Mech. Sin. **31**, 799 (2015).
31 C. Xia, H. Wang, X. Shan, Z. Yang, and Q. Li, Effects of ground configurations on the slipstream and near wake of a high-speed train, J. Wind Eng. Industrial AeroDyn. **168**, 177 (2017).
32 J. Wang, G. Minelli, X. Miao, J. Zhang, T. Wang, G. Gao, and S. Krajnović, The effect of bogie positions on the aerodynamic behavior of a high-speed train. An IDDES study, Flow Turbul. Combust. **107**, 257 (2021).
33 Wind tunnel test report for a new generation of high-speed trains. CRRC Qingdao Sifang Co., Ltd., 2009.
34 C. Xia, X. Z. Shan, and Z. G. Yang, Comparison of different ground simulation systems on the flow around a high-speed train, J. Rail& Rapid Transit. **231**, 135 (2017).
35 C. Baker, The flow around high speed trains, J. Wind Eng. Ind. Aerodyn. **98**, 277 (2010).

底部导流板对高速列车气动减阻的影响

刘　雯, 纪占玲, 郭迪龙, 杨国伟, 周高伟, 任坤华

摘要　转向架和车下设备区域是高速列车气动阻力的主要来源之一. 基于此, 本文提出一种安装于转向架舱前后端的小型导流板装置, 以改善列车的底部流动、减小列车的气动阻力. 采用IDDES方法对是否安装底部导流板的不同列车模型开展非定常数值仿真, 并对导流板的减阻效果和作用机理进行分析. 结果表明: 底部导流板可以将列车底部高速气流导向地面, 减小气流对转向架及车下设备的冲击作用, 从而产生显著的气动减阻效果. 此外, 还讨论了底部导流板不同安装位置对减阻效果的影响, 最终得到了实现整车减阻约12%的一种最佳安装方式. 同时, 导流板还能够减小底部流场在展向上的影响范围, 减小列车风, 这对铁路沿线工人和平台等候乘客的安全具有更高保障. 本研究为高速列车气动减阻提供了新思路、新方法, 对节能减耗、可持续发展等具有重要意义.